Supporting Information

Mechanistic Insights into Oxidation Induced Size Conversion of $[Au_6(dppp)_4]^{2+}$ to $[Au_8(dppp)_4Cl_2]^{2+}$

*S*huping *He,*[a] *Y*ing *Lv,*[a] *X*iaohang *Wu,*[a] *Yan Zhao,*[b,c] *H*aizhu *Yu.*[*,a,b]

a Department of Chemistry and Centre for Atomic Engineering of Advanced Materials, Anhui Province Key Laboratory of Chemistry for Inorganic/Organic Hybrid Functionalized Materials, Key Laboratory of Structure and Functional Regulation of Hybrid Materials of Ministry of Education, Anhui University, Hefei, Anhui, 230601 P. R. China.

b Institute of Energy, Hefei Comprehensive National Science Center, Hefei, Anhui, P. R. China.

c School of Material Engineering and Science, Anhui University of Science and Technology, Huainan, Anhui 232000, P. R. China.

Email: yuhaizhu@ahu.edu.cn.

Contents:

1. Reaction equation

$M + 0.5\ H_2O_2 \rightarrow M^+ + OH^-$

$M + Cl^- \rightarrow MCl^-$

(M: donated cluster intermediates**)**

2. Detailed calculation results on the Au_6 activation stage

2.1. The preliminary transformation of $[Au_6(dmpp)_4]^{2+}$

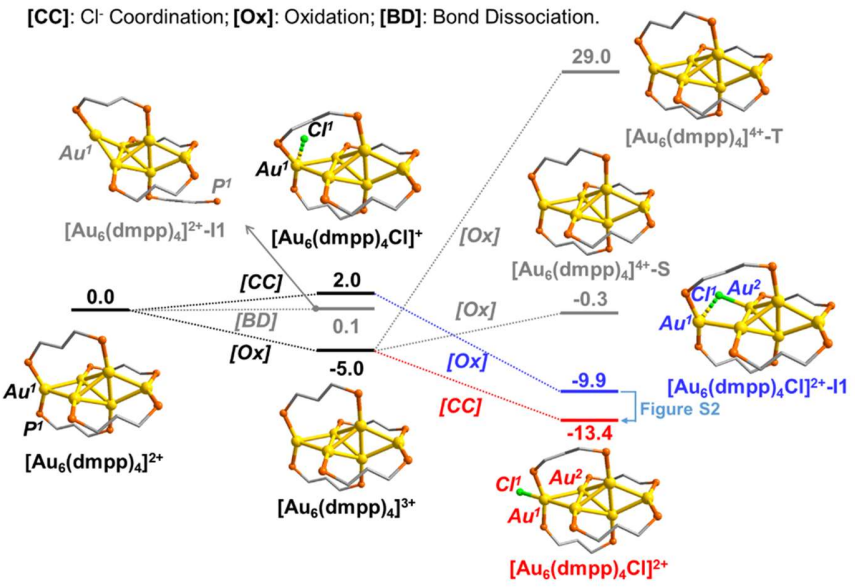

Figure S1. The energy profiles for the transformation of $[Au_6(dmpp)_4]^{2+}$ starting with the Au-P bond dissociation ([BD]), Cl^- coordination ([CC]), and oxidation ([Ox]) steps. The methyl groups on P and H atoms are omitted for clarity. The relative bond energy is given in kcal/mol.

According to the results in Figure S1, the coordination of Cl^- and Au-P dissociation directly on $[Au_6(dmpp)_4]^{2+}$ are endothermic by 2.0 and 0.1 kcal/mol, respectively. Meanwhile, the oxidation of $[Au_6(dmpp)_4]^{2+}$ to $[Au_6(dmpp)_4]^{3+}$ by H_2O_2 is exothermic by 5.0 kcal/mol. Further oxidation of the radical species $[Au_6(dmpp)_4]^{3+}$ to either a singlet or triplet state ($[Au_6(dmpp)_4]^{4+}$**-S/T**, and S, T denote singlet, triplet) is less feasible than the Cl^- coordination step ($[Au_6(dmpp)_4]^{3+} + Cl^- \rightarrow$

$[Au_6(dmpp)_4Cl]^{2+}$). Interestingly, the relative energy of $[Au_6(dmpp)_4Cl]^{2+}$ is 3.5 kcal/mol lower in energy than its isomer $[Au_6(dmpp)_4Cl]^{2+}$-I1 (I denotes isomer). A detailed analysis by fixing the Au^2-Cl^1 bond at different distances indicates a gradual energy decrease until the formation of $[Au_6(dmpp)_4Cl]^{2+}$ (Figure S2). Therefore, the latter transformations of both $[Au_6(dmpp)_4Cl]^{2+}$ and $[Au_6(dmpp)_4Cl]^{2+}$-I1 were taken into account.

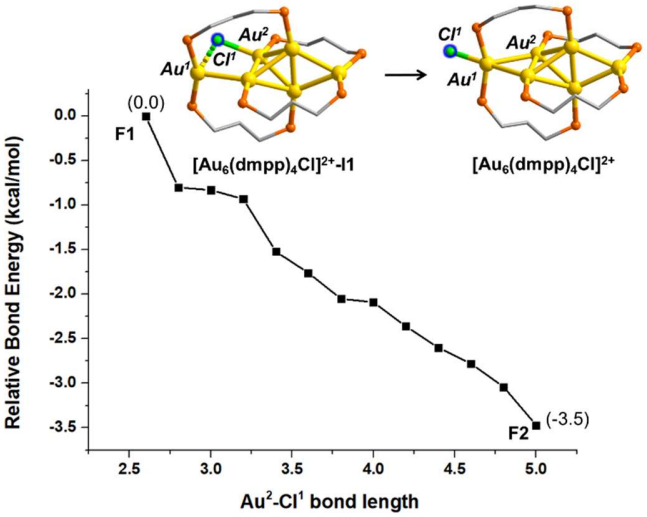

Figure S2. The energy (in kcal/mol) profile for the transformation from $[Au_6(dmpp)_4Cl]^{2+}$-I1 to $[Au_6(dmpp)_4Cl]^{2+}$ via a partial optimization by fixing the Au^2-Cl^1 bond at selected distances. The methyl groups on dmpp and all H atoms are omitted for clarity.

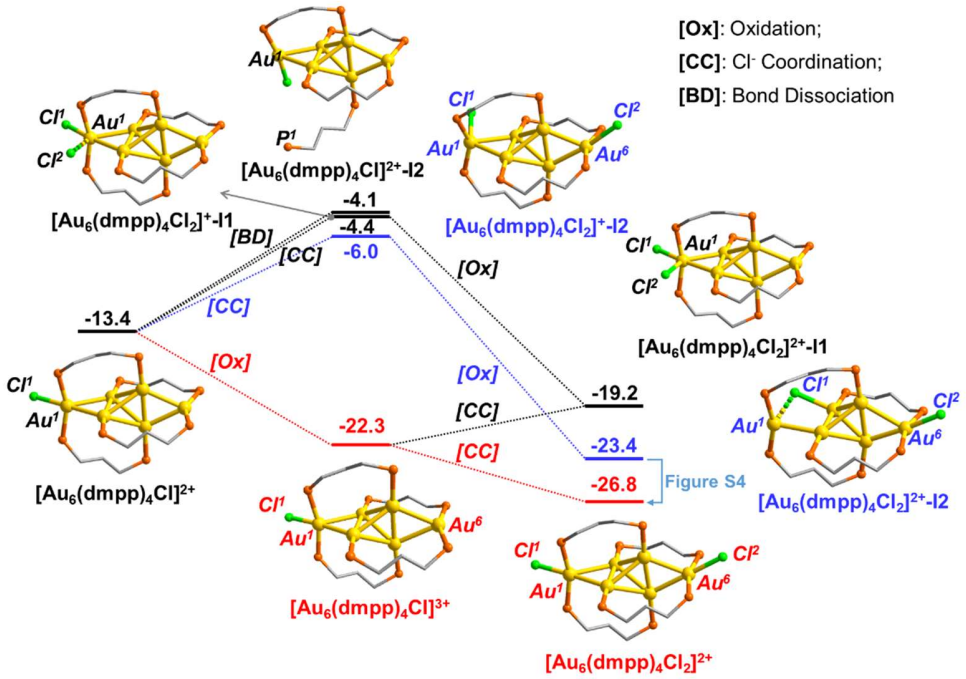

Figure S3. Energy profiles for the Cl^- coordination, oxidation and Au-P bond dissociation steps from $[Au_6(dmpp)_4Cl]^{2+}$. For clarity, the methyl group on dmpp and all the H atoms are omitted. The relative bond energies are given in kcal/mol.

From $[Au_6(dmpp)_4Cl]^{2+}$, the Au^1-P^1 dissociation is less feasible than the coordination of the second Cl^-, or the second oxidation steps. Meanwhile, the relative energy of the oxidation product $[Au_6(dmpp)_4Cl]^{3+}$ is remarkably lower than that of second Cl^- coordinated intermediates $[Au_6(dmpp)_4Cl_2]^+$-I1/I2. From $[Au_6(dmpp)_4Cl]^{3+}$, the second Cl^- favorably coordinates to the other corner Au atom (i.e. Au^6) to form $[Au_6(dmpp)_4Cl_2]^{2+}$, instead of coordinating to the Au^1 atom to form $[Au_6(dmpp)_4Cl_2]^{2+}$-I1. By contrast, an alternative Cl^- coordination-oxidation pathway (forming $[Au_6(dmpp)_4Cl_2]^{2+}$-I1/I2) is less likely. The two chlorides adopt the coordination mode of (μ_2-, μ_1-) and (μ_1-, μ_1-) in $[Au_6(dmpp)_4Cl_2]^{2+}$-I2 and $[Au_6(dmpp)_4Cl_2]^{2+}$, respectively. Similar to

the aforementioned results, the structure bearing one μ_2-coordinated Cl is less stable, and the isomerization between the μ_1- and μ_2- is very easy (Figure S4).

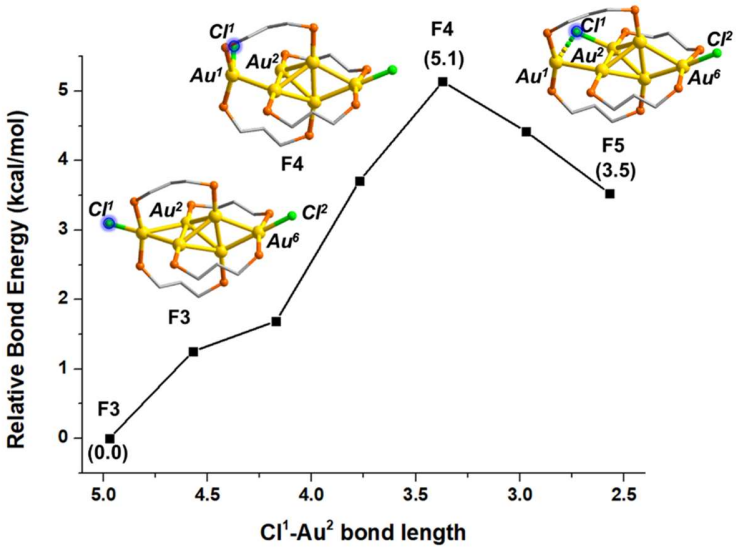

Figure S4. Bond energy (in kcal/mol) profile for the isomerization of $[Au_6(dmpp)_4Cl_2]^{2+}$ to $[Au_6(dmpp)_4Cl_2]^{2+}$-I2 determined by partial optimization via fixing the Au^2-Cl^1 distance at different value (in between that of $[Au_6(dmpp)_4Cl_2]^{2+}$ to $[Au_6(dmpp)_4Cl_2]^{2+}$-I2).

2.2. The energy changes for the 3rd oxidation/Cl⁻ coordination steps

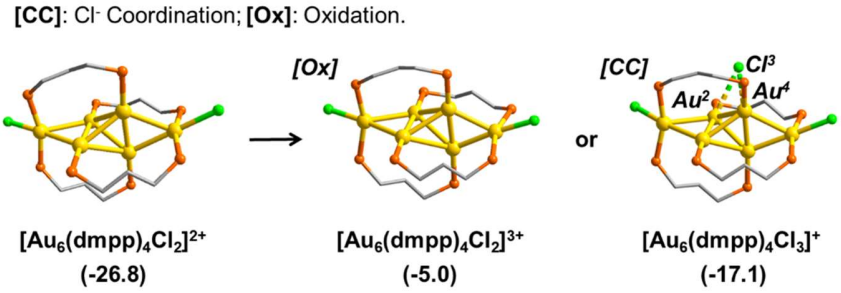

Figure S5. The bond energy and optimized geometry of the intermediate after the coordination of the third oxidation step ($[Au_6(dmpp)_4Cl_2]^{3+}$) or the third Cl^- ($[Au_6(dmpp)_4Cl_3]^{+}$) from $[Au_6(dmpp)_4Cl_2]^{2+}$. The relative energies are given in kcal/mol. The relative energy of

$[Au_6(dmpp)_4Cl_2]^{3+}$ is higher than all species in the decomposition pathway, while the third Cl coordination is mainly precluded from the weak interactions therein (the Cl^3-Au^2/Au^4 distances are 3.24/3.08 Å, and significantly longer than the ~2.5 Å distance of Au-Cl bond).

3. Detailed calculation results on the Au_6 decomposition stage

3.1. The energy profiles for Au-Au/Au-P dissociation steps from $[Au_6(dmpp)_4Cl_2]^{2+}$

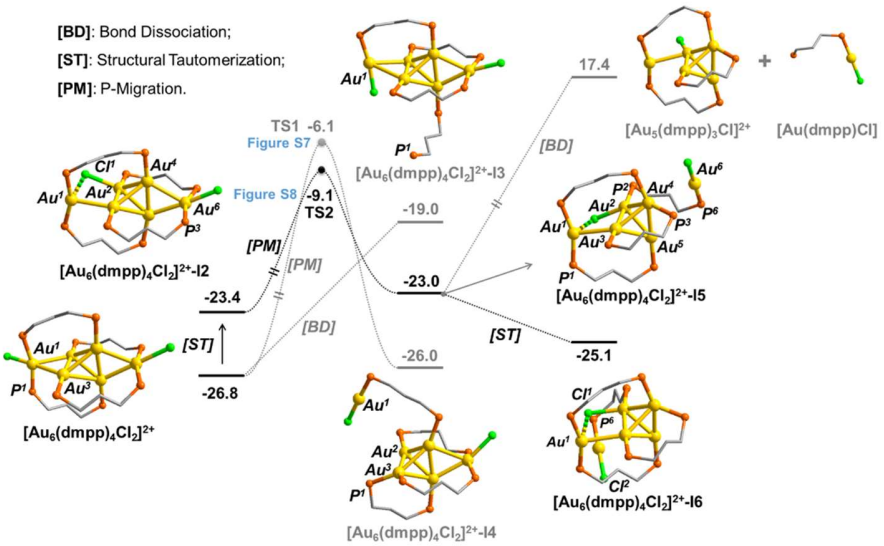

Figure S6. The bond energy profiles for the Au-P dissociation and structure tautomerization steps from **$[Au_6(dmpp)_4Cl_2]^{2+}$**. The relative energies are given in kcal/mol.

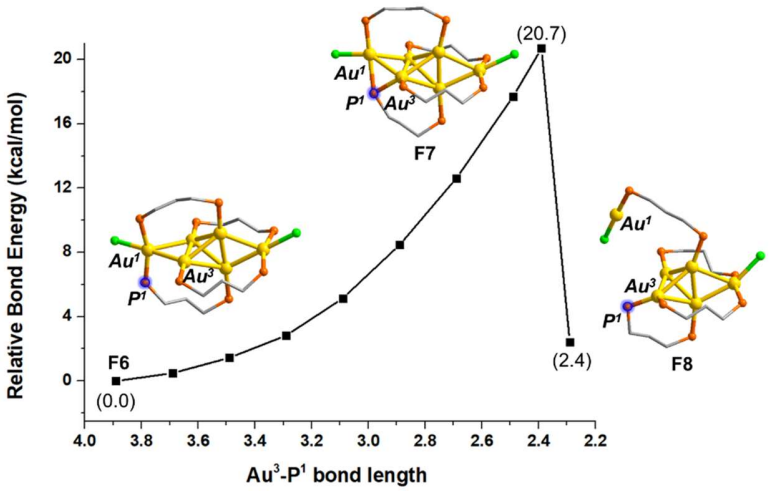

Figure S7. The bond energy (in kcal/mol) profile for the transformation from $[Au_6(dmpp)_4Cl_2]^{2+}$ to $[Au_6(dmpp)_4]^{2+}$-I4 via partial optimization analysis (fixing Au^4-P^1 bond at different distances).

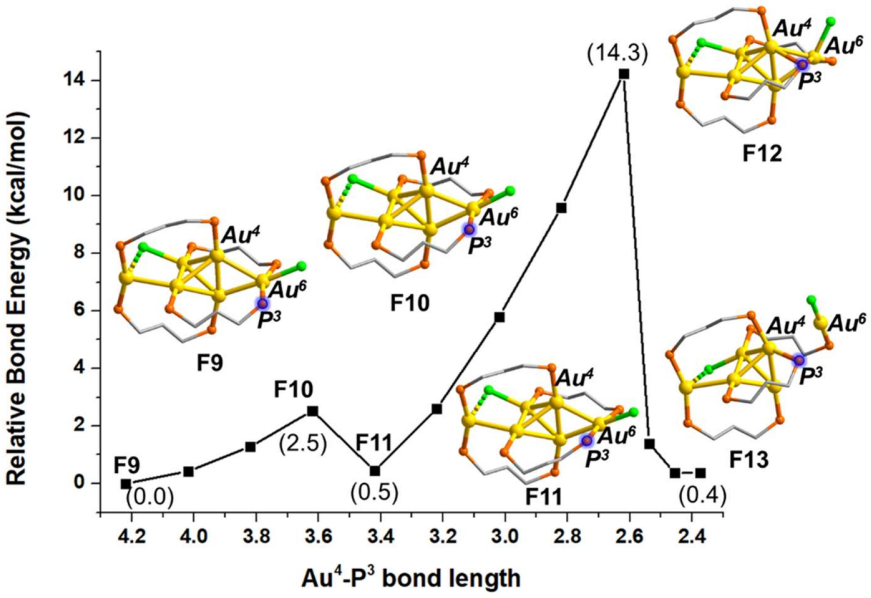

Figure S8. The bond energy (in kcal/mol) profile for the transformation from $[Au_6(dmpp)_4]^{2+}$-I2 to $[Au_6(dmpp)_4]^{2+}$-I5 via partial optimization analysis (fixing Au^4-P^3 bond at different distances).

3.2 Structural tautomerization steps prior to the Au_2+Au_4 decomposition

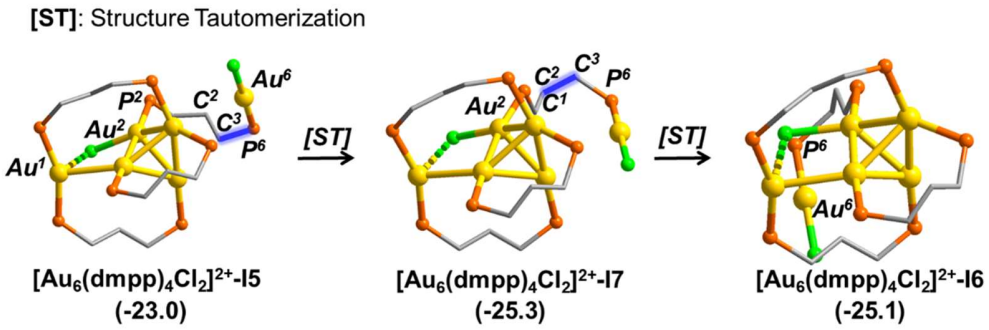

Figure S9. The structure and energy changes from $[Au_6(dmpp)_4Cl_2]^{2+}$-I5 to $[Au_6(dmpp)_4Cl_2]^{2+}$-I6. $[Au_6(dmpp)_4Cl_2]^{2+}$-I7 can be obtained by rotating the Au^6-P^6 moiety along the C^3-P^6 bond, which can lower the surrounding steric hindrance. After that, rotating the C^3-P^6 bond along the C^3-C^2 bond results in the intermediate $[Au_6(dmpp)_4Cl_2]^{2+}$-I6. The relative energies are given in kcal/mol.

3.3 The energy changes for the different Au_2+Au_4 decomposition modes

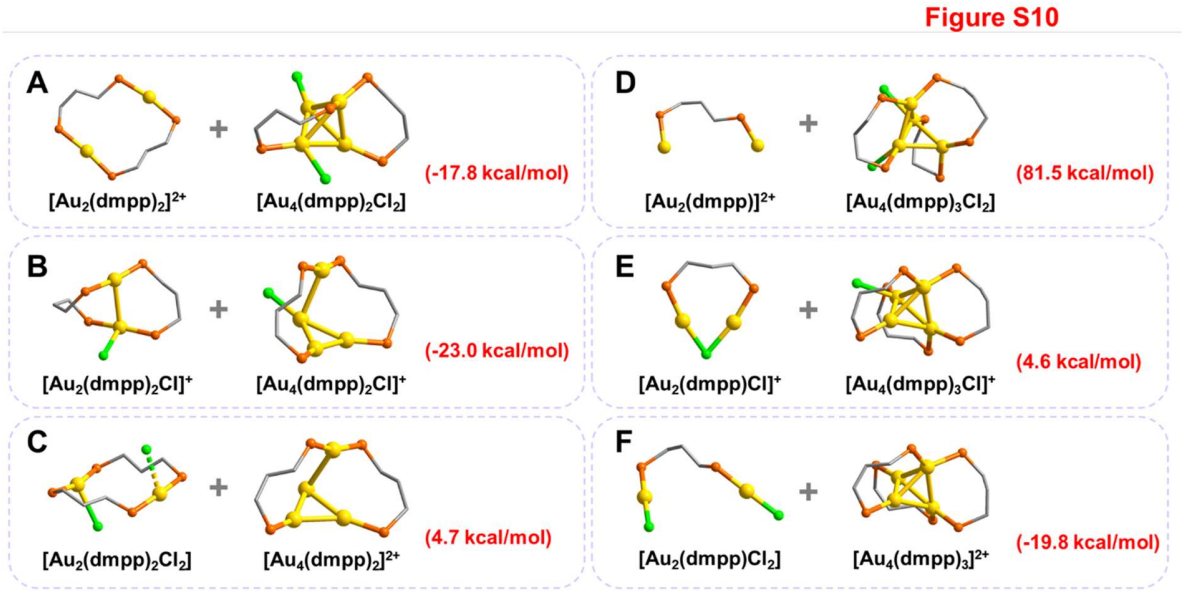

Figure S10. The relative energy (in kcal/mol) and optimized geometry of six possible products from **$[Au_6(dmpp)_4Cl_2]^{2+}$-I16**.

3.4 The energy profiles for formation of {$[Au_2(dmpp)_2Cl]^+$ + $[Au_4(dmpp)_2Cl]^+$}

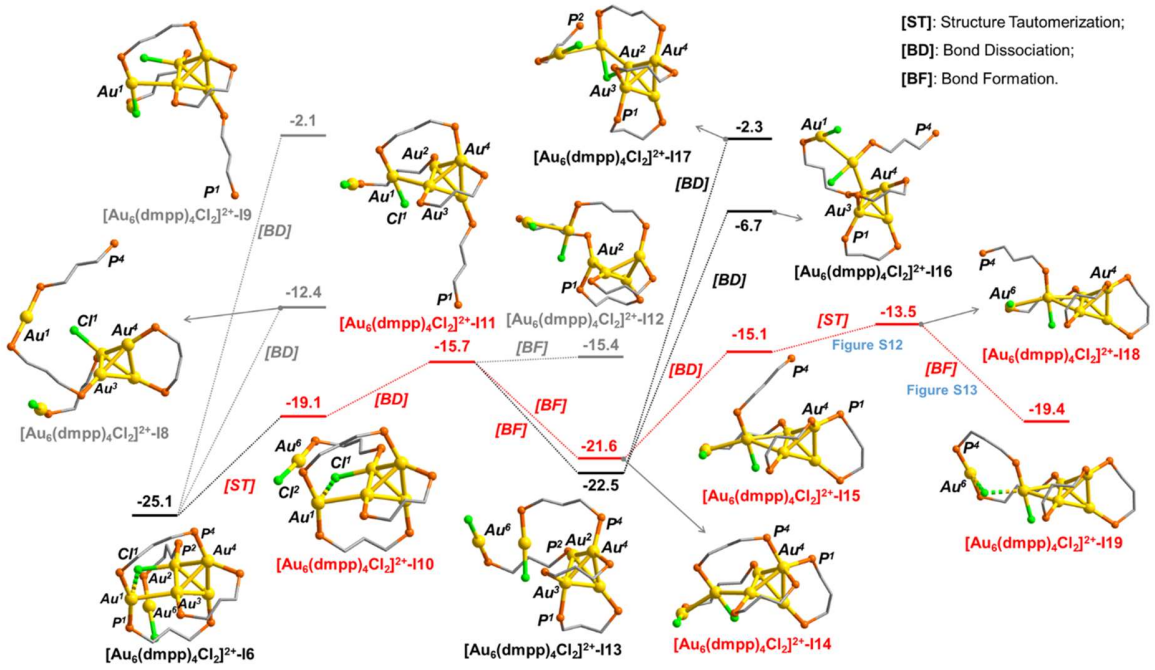

Figure S11. The bond energy profiles for the Au-P dissociation, $Au^{2/3/4}$-P^1 formation and the formation of first bridging dmpp in Au_2 fragment from $[Au_6(dmpp)_4Cl_2]^{2+}$-I6. The relative energies are given in kcal/mol.

From **$[Au_6(dmpp)_4Cl_2]^{2+}$-I6**, the direct Au^4-P^4 cleavage to **$[Au_6(dmpp)_4Cl_2]^{2+}$-I8** or Au^1-P^1 cleavage to form **$[Au_6(dmpp)_4Cl_2]^{2+}$-I9** are both more energy-demanding compared to the tautomerization-Au^1-P^1 cleavage step (**$[Au_6(dmpp)_4Cl_2]^{2+}$-I6→$[Au_6(dmpp)_4Cl_2]^{2+}$-I10→$Au_6(dmpp)_4Cl_2]^{2+}$-I11**). Thereafter, three types of P-Au bond formation (P^1-$Au^{2/3/4}$) could possibly occur. The P^1-Au^2 formation is less feasible than that of P^1-$Au^{3/4}$ (**$[Au_6(dmpp)_4Cl_2]^{2+}$-I12 vs $[Au_6(dmpp)_4Cl_2]^{2+}$-I13/I14**), predominantly due to the weakening of the metallic bonding interactions in the Au_4 core. From either **$[Au_6(dmpp)_4Cl_2]^{2+}$-I13** or **$[Au_6(dmpp)_4Cl_2]^{2+}$-I14**, Au^4-P^4 dissociation is prerequisite to the P^4-Au^6 formation step to constitute the first bridging dmpp between Au_1 and Au_6 atoms. Due to the relatively higher coordination number of Au^4 in **$[Au_6(dmpp)_4Cl_2]^{2+}$-I14** than that of **$[Au_6(dmpp)_4Cl_2]^{2+}$-I13**, Au^4-P^4 cleavage in the former case

is more feasible. After that, P^4-Au^6 formation occurs via a stepwise structural tautomerization (with energy barrier of 5.2 kcal/mol, Figure S12) and bond formation (barrier 4.0 kcal/mol, Figure S13) process to form the intermediate **$[Au_6(dmpp)_4Cl_2]^{2+}$-I19**.

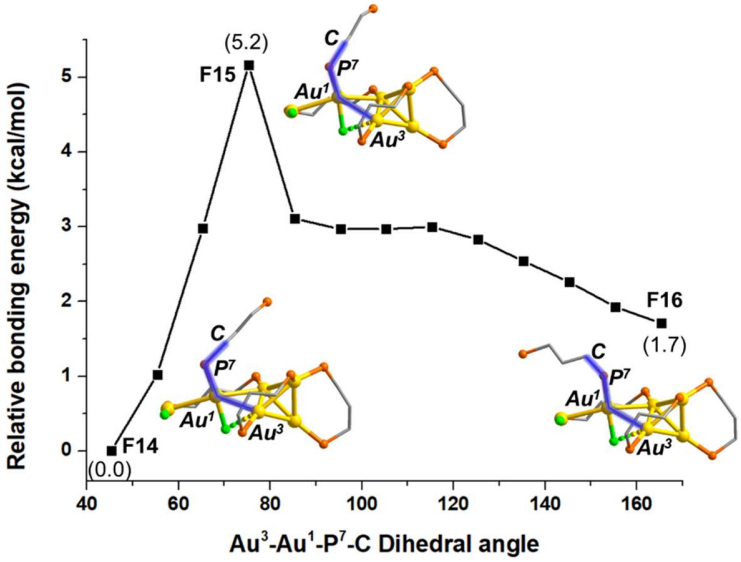

Figure S12. The bond energy (in kcal/mol) profile for the transformation from **$[Au_6(dmpp)_4Cl_2]^{2+}$-I15** to **$[Au_6(dmpp)_4Cl_2]^{2+}$-I18** via partial optimization analysis (fixing Au^3-Au^1-P^7-C at different dihedral angle).

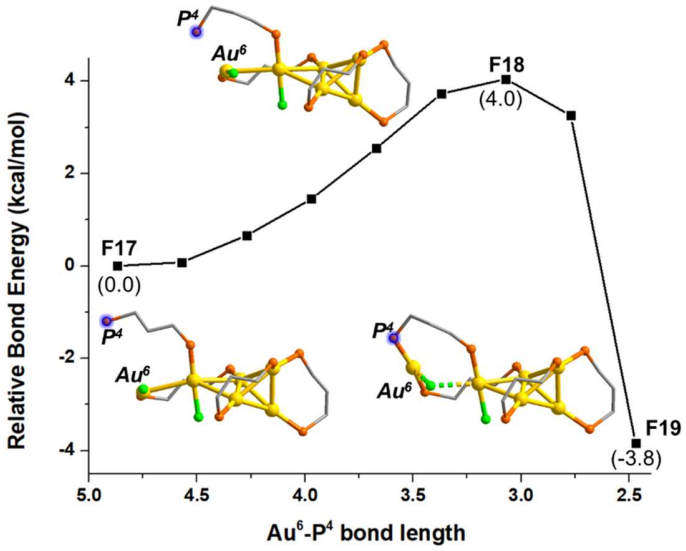

Figure S13. The bond energy (in kcal/mol) profile for the transformation from **$[Au_6(dmpp)_4Cl_2]^{2+}$-I18** to **$[Au_6(dmpp)_4Cl_2]^{2+}$-I19** via partial optimization analysis (fixing Au^6-P^4 bond at different distances).

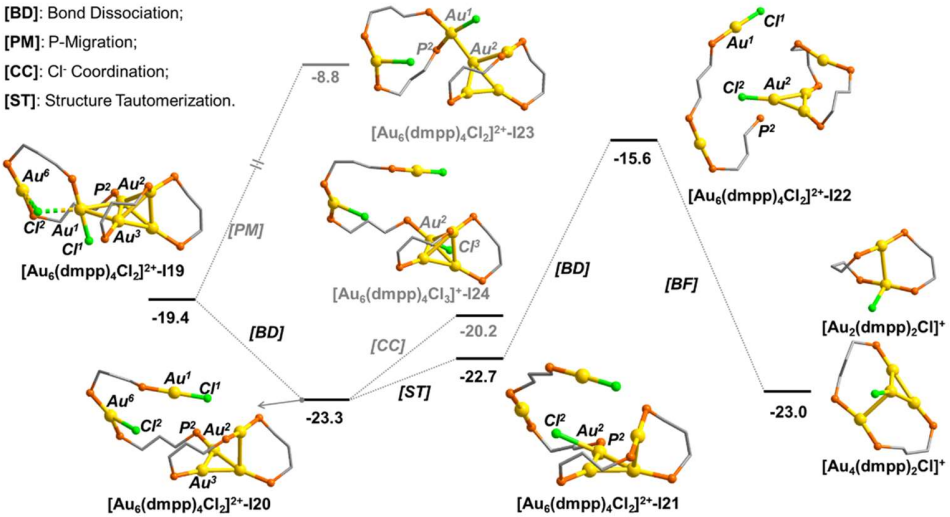

Figure S14. The bond energy profiles from **$[Au_6(dmpp)_4Cl_2]^{2+}$-I19** to form two independent Au_2 and Au_4 blocks. The relative energies are given in kcal/mol. The high energy of **$[Au_6(dmpp)_4Cl_2]^{2+}$-I23** is mainly caused by the presence of a bare surface Au^2, while the Au^2 coordination with an extra Cl^- (forming **$[Au_6(dmpp)_4Cl_2]^{2+}$-I24**) is less feasible than the direct Cl^2-migration step. The exothermicity of **$[Au_6(dmpp)_4Cl_2]^{2+}$-I19** to **$[Au_6(dmpp)_4Cl_2]^{2+}$-I20** is mainly caused by the increased core electron density of Au_4 moiety (the Hirshfeld charge: 0.106 vs 0.057).

4. Detailed calculation results on the dimerization stage

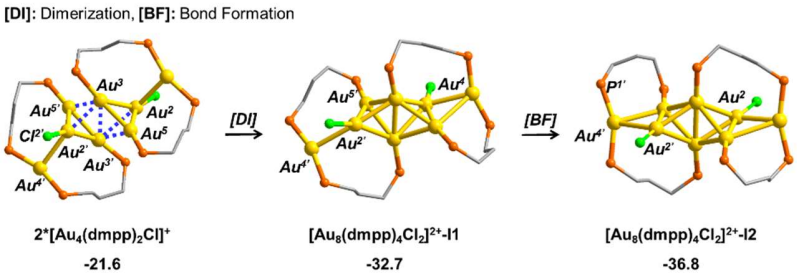

Figure S15. The detailed changes in atomic structure and relative energy profiles from $[Au_4(dmpp)_2Cl]^+$ to **$[Au_8(dmpp)_4Cl_2]^{2+}$-I2**. The relative energies are given in kcal/mol.

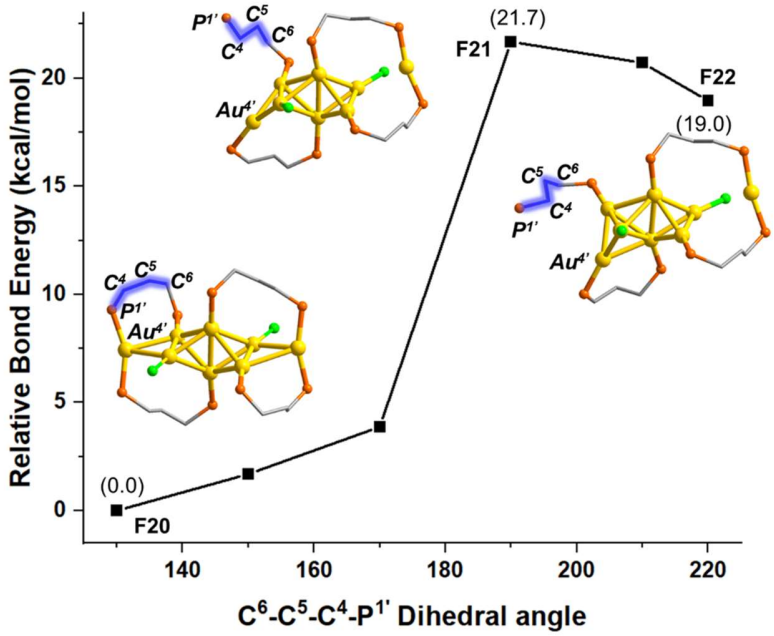

Figure S16. The bond energy (in kcal/mol) profile for the transformation from $[Au_8(dmpp)_4Cl_2]^{2+}$-I2 to $[Au_8(dmpp)_4Cl_2]^{2+}$–I3 via partial optimization analysis (fixing C^6-C^5-C^4-$P^{1'}$ bond at different dihedral angle).

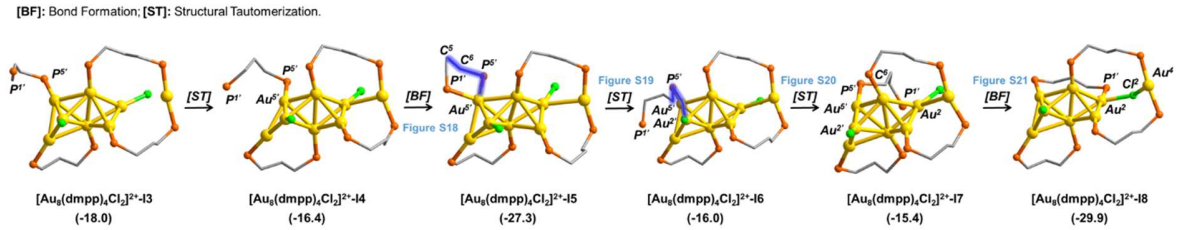

Figure S17. The structure and energy changes from **$[Au_8(dmpp)_4Cl_2]^{2+}$-I3** to **$[Au_8(dmpp)_4Cl_2]^{2+}$-I8**. The relative energies are given in kcal/mol.

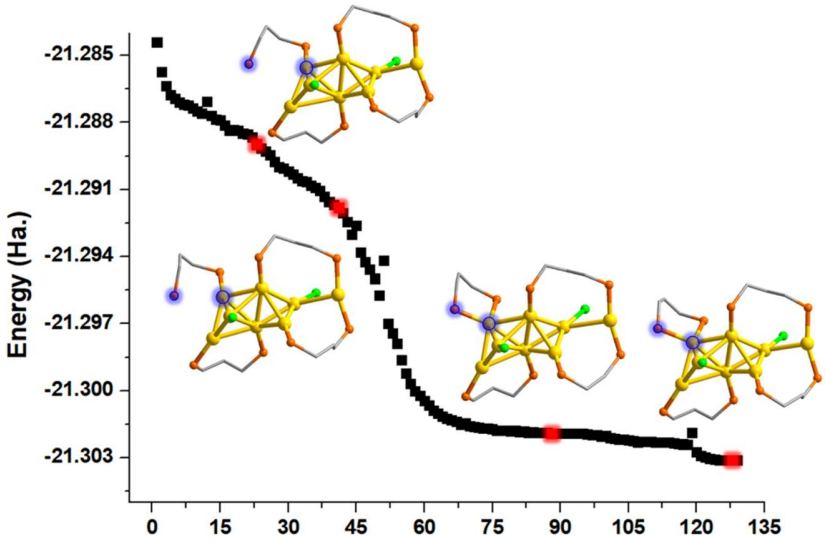

Figure S18. Geometry optimization energy profile of **$[Au_8(dmpp)_4Cl_2]^{2+}$-I4** and the selected intermediate structures.

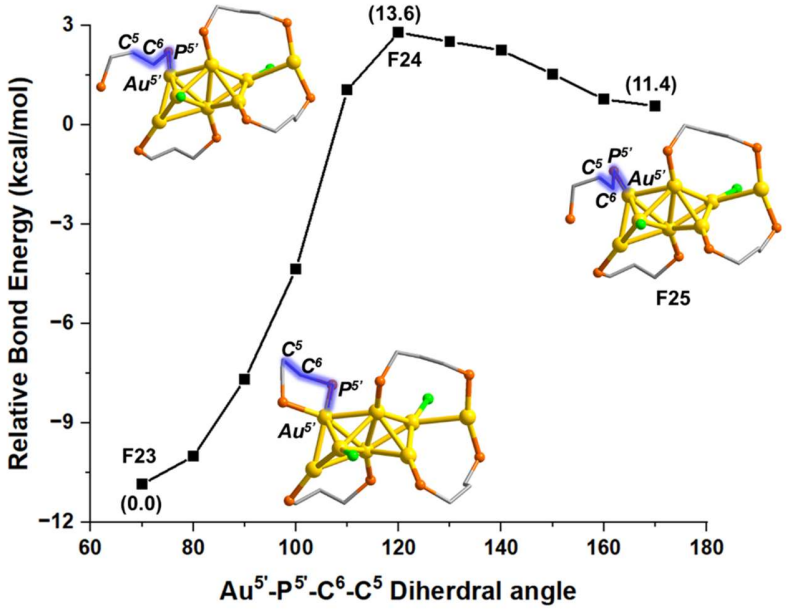

Figure S19. The bond energy (in kcal/mol) profile for the transformation from $[Au_8(dmpp)_4Cl_2]^{2+}$-I5 to $[Au_8(dmpp)_4Cl_2]^{2+}$-I6 via partial optimization analysis (fixing $Au^{5'}$-$P^{5'}$-C^6-C^5 bond at different dihedral angle).

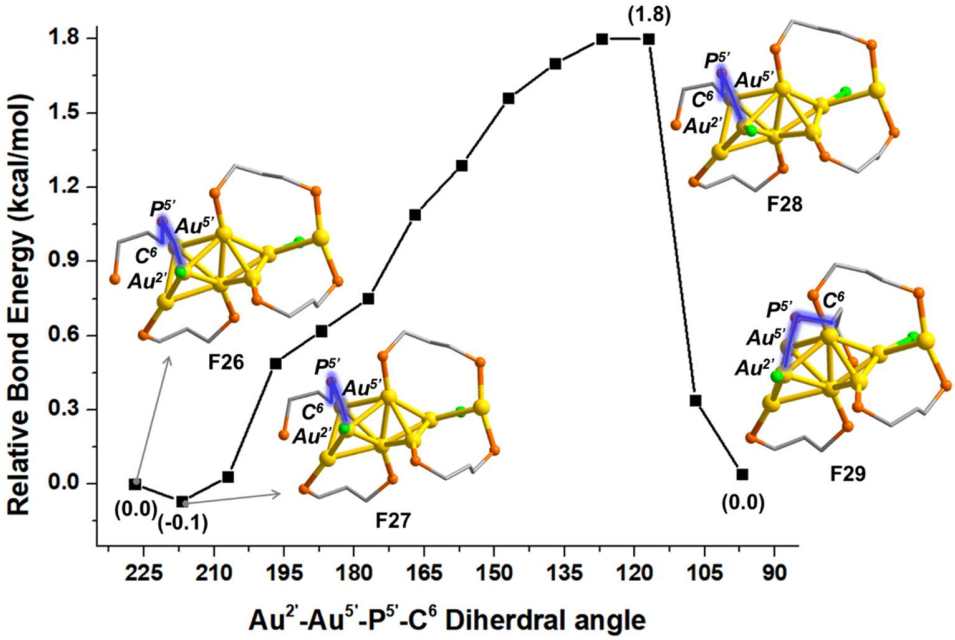

Figure S20. The bond energy (in kcal/mol) profile for the transformation from $[Au_8(dmpp)_4Cl_2]^{2+}$-I6 to $[Au_8(dmpp)_4Cl_2]^{2+}$-I7 via partial optimization analysis (fixing $Au^{2'}$-$Au^{5'}$-$P^{5'}$-C^6 bond at different dihedral angle).

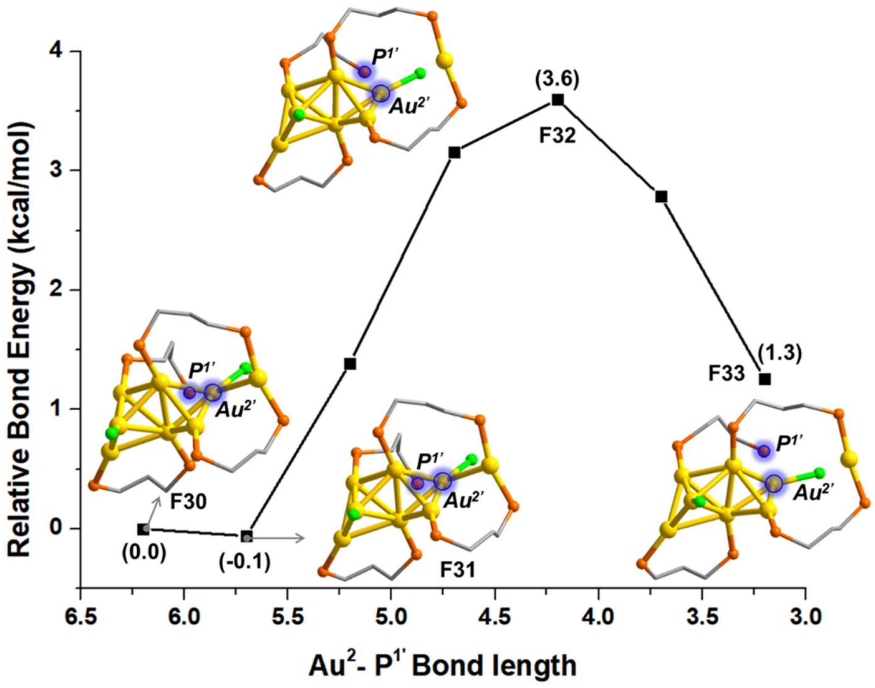

Figure S21. The bond energy (in kcal/mol) profile for the transformation from $[Au_8(dmpp)_4Cl_2]^{2+}$-I7 to $[Au_8(dmpp)_4Cl_2]^{2+}$-I8 via partial optimization analysis (fixing Au^2-$P^{1'}$ bond at different distances).

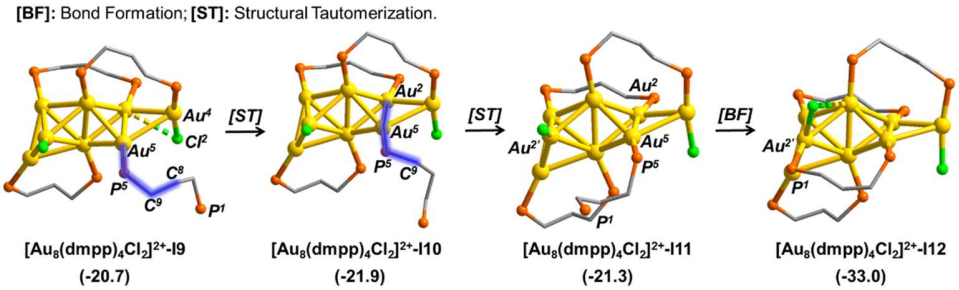

Figure S22. The structure and energy changes from **$[Au_8(dmpp)_4Cl_2]^{2+}$-I9** to **$[Au_8(dmpp)_4Cl_2]^{2+}$-I12**. The relative energies are given in kcal/mol.

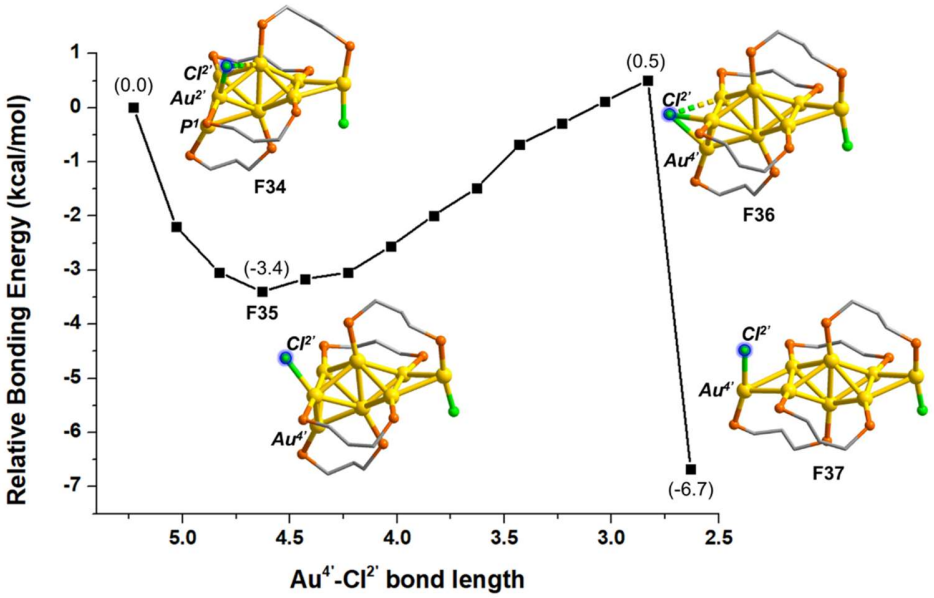

Figure S23. The bond energy (in kcal/mol) profile for the transformation from $[Au_8(dmpp)_4Cl_2]^{2+}$-I12 to the final product $[Au_8(dmpp)_4Cl_2]^{2+}$ via partial optimization analysis (fixing $Au^{4'}$-$Cl^{2'}$ bond at different distances).

5. GUM analysis on the reaction site of the key cluster species

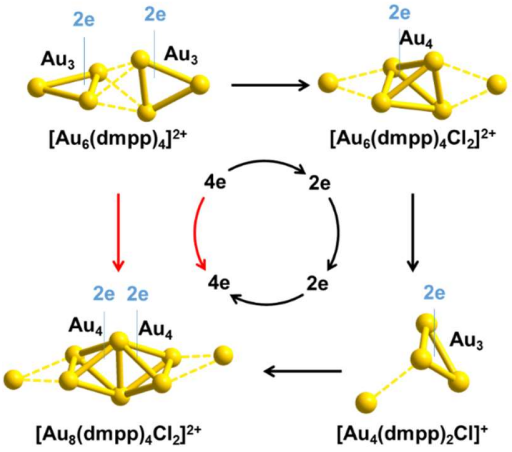

Figure S24. The structural analysis of the four key species during the conversion of $[Au_6(dmpp)_4]^{2+}$ to $[Au_8(dmpp)_4Cl_2]^{2+}$ with GUM model.

6. Frequency calculation results.

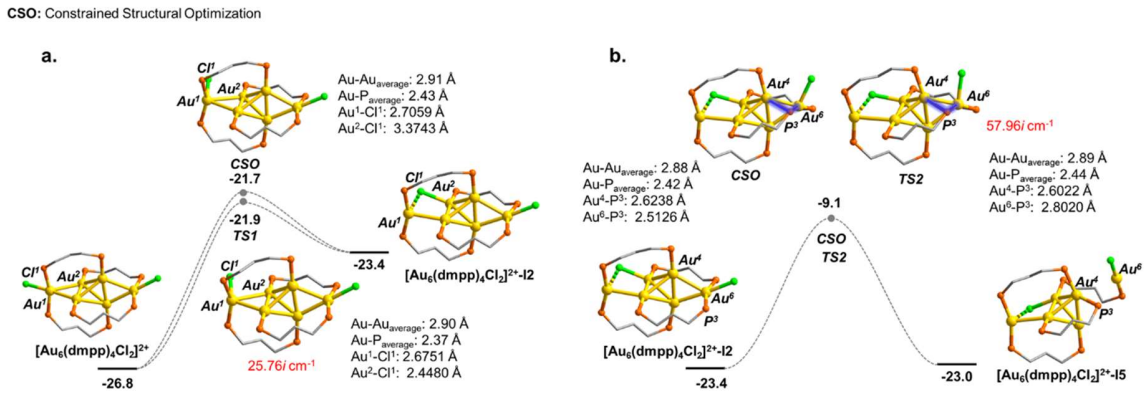

Figure S25. The bond energy profiles of the transformation of **$[Au_6(dmpp)_4Cl_2]^{2+}$** → **$[Au_6(dmpp)_4Cl_2]^{2+}$-I2** (a), and **$[Au_6(dmpp)_4Cl_2]^{2+}$-I2** → **$[Au_6(dmpp)_4Cl_2]^{2+}$-I5** (b), with the structure and energy of the transition state structure determined by partial optimization curve analysis (denoted as CSO) and the full transition state optimization (denoted as **TS1**/**TS2**). The relative energies are given in kcal/mol.

Table S1. The relative electronic energy (ΔE, kcal/mol) and the relative Gibbs free energy (ΔG, kcal/mol) of some intermediates. The relative energies are given in kcal/mol.

	ΔE (kcal/mol)	**ΔG (kcal/mol)**		**ΔE (kcal/mol)**	**ΔG (kcal/mol)**
$[Au_6(dmpp)_4Cl_2]^{2+}$	-	-	$[Au_8(dmpp)_4Cl_2]^{2+}$-I1	-	-
$[Au_6(dmpp)_4Cl_2]^{2+}$-I2	3.5	4.2	$[Au_8(dmpp)_4Cl_2]^{2+}$-I2	-4.1	-3.7
$[Au_6(dmpp)_4Cl_2]^{2+}$-I5	3.9	7.7	$[Au_8(dmpp)_4Cl_2]^{2+}$-I3	14.8	12.2
$[Au_6(dmpp)_4Cl_2]^{2+}$-I6	1.8	2.9	$[Au_8(dmpp)_4Cl_2]^{2+}$-I4	16.3	16.1
$[Au_6(dmpp)_4Cl_2]^{2+}$-I7	1.6	4.4	$[Au_8(dmpp)_4Cl_2]^{2+}$-I5	5.4	4.2
$[Au_6(dmpp)_4Cl_2]^{2+}$-I10	7.8	8.5	$[Au_8(dmpp)_4Cl_2]^{2+}$-I6	16.8	17.5
$[Au_6(dmpp)_4Cl_2]^{2+}$-I11	11.1	11.3	$[Au_8(dmpp)_4Cl_2]^{2+}$-I7	16.8	17.4
$[Au_6(dmpp)_4Cl_2]^{2+}$-I14	5.2	7.0	$[Au_8(dmpp)_4Cl_2]^{2+}$-I8	2.8	1.4
$[Au_6(dmpp)_4Cl_2]^{2+}$-I15	11.8	13.7	$[Au_8(dmpp)_4Cl_2]^{2+}$-I9	12.0	8.5
$[Au_6(dmpp)_4Cl_2]^{2+}$-I18	13.3	12.9	$[Au_8(dmpp)_4Cl_2]^{2+}$-I10	10.8	9.0
$[Au_6(dmpp)_4Cl_2]^{2+}$-I19	7.5	7.4	$[Au_8(dmpp)_4Cl_2]^{2+}$-I11	11.4	9.6
$[Au_6(dmpp)_4Cl_2]^{2+}$-I20	3.6	8.7	$[Au_8(dmpp)_4Cl_2]^{2+}$-I12	-0.3	-1.6
$[Au_6(dmpp)_4Cl_2]^{2+}$-I21	4.2	7.8	$[Au_8(dmpp)_4Cl_2]^{2+}$	-11.7	-14.8
$[Au_6(dmpp)_4Cl_2]^{2+}$-I22	10.8	13.9			
TS1	5.0	6.6			
TS2	17.7	19.5			

7. Configuration analysis.

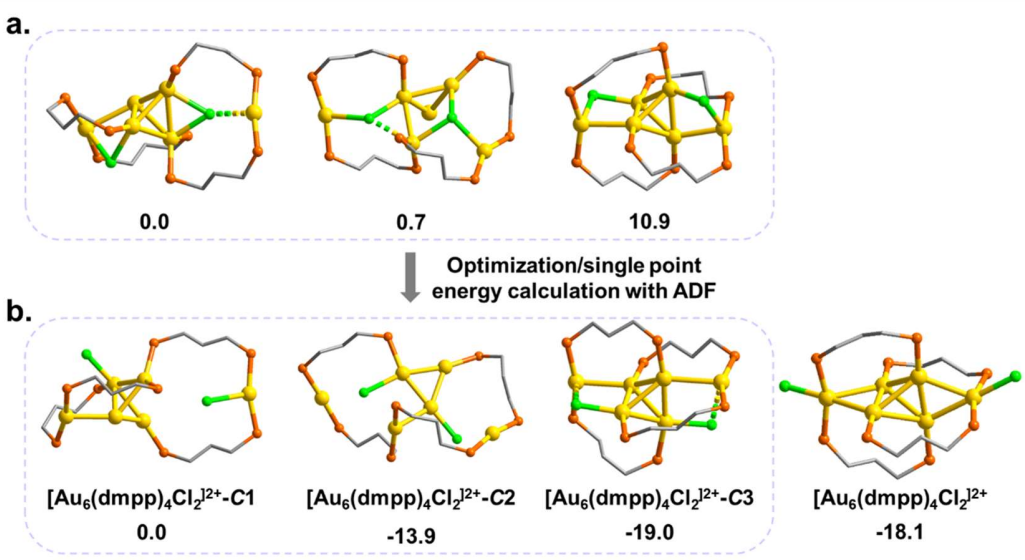

Figure S26. The geometry and relative energy of **[Au$_6$(dmpp)$_4$Cl$_2$]$^{2+}$-*C*1, [Au$_6$(dmpp)$_4$Cl$_2$]$^{2+}$-*C*2, [Au$_6$(dmpp)$_4$Cl$_2$]$^{2+}$-*C*3**, and **[Au$_6$(dmpp)$_4$Cl$_2$]$^{2+}$**. The relative energies are given in kcal/mol.

Herein, the configuration analysis of **[Au$_6$(dmpp)$_4$Cl$_2$]$^{2+}$** structure (the most stable Au$_6$ intermediate) was used as an example. With the GFN2-xTB analysis, three structures **[Au$_6$(dmpp)$_4$Cl$_2$]$^{2+}$-*C*1/*C*2** (the two with the lowest energy) and **[Au$_6$(dmpp)$_4$Cl$_2$]$^{2+}$-*C*3** (which is structurally similar to **[Au$_6$(dmpp)$_4$Cl$_2$]$^{2+}$**) were screened, and their relative energy is shown in Figure S26a. After ADF calculations (geometry optimization and single point energy calculations as mentioned in the article), the relative energy of these structures changes significantly and the relative energy of both **[Au$_6$(dmpp)$_4$Cl$_2$]$^{2+}$-*C*1** and **[Au$_6$(dmpp)$_4$Cl$_2$]$^{2+}$-*C*2** are significantly higher that of **[Au$_6$(dmpp)$_4$Cl$_2$]$^{2+}$** (Figure S26b). Meanwhile, the relative energy of **[Au$_6$(dmpp)$_4$Cl$_2$]$^{2+}$-*C*3** is slightly lower than that of **[Au$_6$(dmpp)$_4$Cl$_2$]$^{2+}$** by only 0.9 kcal/mol, indicating that the two isomers could exist in equilibrium. The aforementioned results indicate that the metal nanocluster

systems might be too tough for GFN2-xTB conformation analysis. More examples and efforts are necessary to finally figure out a suitable conformation analysis method.

8. Calculations with the experimentally used dppp ligands

Figure S27. The energy changes for the oxidation and Cl-coordination steps from the Au6 reactants in presence of the full dppp and the simplified dmpp ligands.

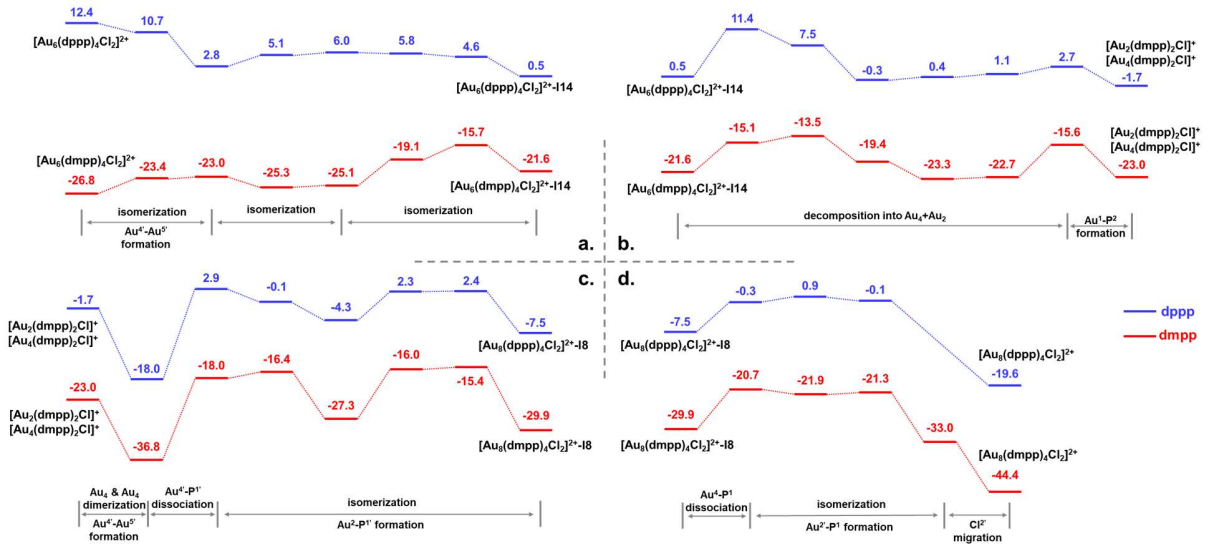

Figure S28. Overview of the mechanism for the oxidation induced size-growth from $[Au_6(dppp)_4Cl_2]^{2+}$ to $[Au_8(dppp)_4Cl_2]^{2+}$. For comparison, the detailed energy profile of the dmpp systems were also given. The relative energies are given in kcal/mol.

9. Structure-property correlation analysis on the Au-P dissociation steps

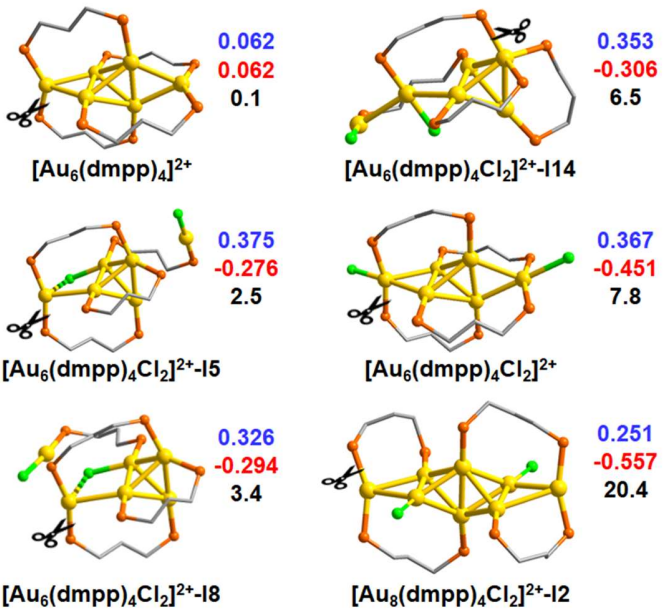

Figure S29. The structure and bond dissociation sites are shown for the six intermediates ($[Au_6(dmpp)_4]^{2+}$, **$[Au_6(dmpp)_4Cl_2]^{2+}$-I5**, **$[Au_6(dmpp)_4Cl_2]^{2+}$-I8**, **$[Au_6(dmpp)_4Cl_2]^{2+}$-I14**, $[Au_6(dmpp)_4Cl_2]^{2+}$, and **$[Au_8(dmpp)_4Cl_2]^{2+}$-I2**). The data gives the Hirshfeld charge of Au_n (blue), Au_nCl_m (red) and $\Delta\Delta E^{BD}$ (black, in kcal/mol) value for each cluster precursor.

10. Structure-property correlation analysis on the oxidation steps

Table S2. The data set of the concerned oxidation precursors.

	VIP(eV)	E_{HOMO}(eV)	N_e	N_{Au}	ave. N_e	N_C	N_L	$N_{M/L}$	$N_{Au\text{-}P/S}$	$N_{Au(0):Au(I)}$	$\Delta\Delta E^{ox}$(eV)
$[Au_6(dmpp)_4Cl_2]^+$-I2	3.70	-3.46	3	6	0.5	1	6	1.00	8	1	-0.75
$[Au_6(dmpp)_4Cl]^+$	3.89	-3.62	4	6	0.67	1	5	1.20	8	2	-0.52
$[Au_6(dmpp)_4Cl]^{2+}$	4.03	-3.77	3	6	0.5	2	5	1.20	8	1	-0.39
$[Au_6(dmpp)_4]^{2+}$	4.22	-3.94	4	6	0.67	2	4	1.50	8	2	-0.22
$[Au_6(dmpp)_4]^{3+}$	4.68	-4.3 8	3	6	0.5	3	4	1.50	8	1	0.20
$[Au_6(dmpp)_4Cl_2]^{2+}$	5.25	-4.99	2	6	0.33	2	6	1.00	8	0.5	0.95
$[Au_8(dppp)_4]^{2+}$	4.79	-4.54	6	8	0.75	2	4	2.00	8	3	0.38
$[Au_8(dppp)_4]^{3+}$	5.19	-4.94	5	8	0.63	3	4	2.00	8	1.7	0.70
$[Au_{23}(c\text{-}C_6)_{16}]^-$	4.21	-4.09	8	23	0.35	-1	16	1.44	32	0.5	-0.13
$[Au_{25}(SMe)_{18}]^-$	4.04	-3.92	8	25	0.32	-1	18	1.39	36	0.5	-0.21
$[Au_{25}(SMe)_{18}]^0$	4.32	-4.20	7	25	0.28	0	18	1.39	36	0.4	-0.11
$[Au_{25}(PET)_{18}]^-$	4.03	-3.95	8	25	0.32	-1	18	1.39	36	0.5	-0.25
$[Au_{25}(PET)_{18}]^0$	4.30	-4.21	7	25	0.28	0	18	1.39	36	0.4	-0.13

VIP: Vertical ionization energies; E_{HOMO}: HOMO energy; N_e: number of free electrons; N_{Au}: Au atom number; ave.N_e: number of free electrons per Au atom, N_C: cluster charge; N_L: number of ligands; $N_{M/L}$: the ratio of metal/ligand; $N_{Au\text{-}P/S}$: the number of metal-ligand bonds (Au-P/S); and $N_{Au(0):Au(I)}$: the ratio of $N_{Au(0)}$: $N_{Au(I)}$; $\Delta\Delta E^{ox}$: the reaction energy of single electron oxidation from DFT calculation.

Table S3. The predicted oxidation reaction energy via the linear correlation (E1-E6) with different variants (all energies are given in eV).

	$\Delta\Delta E^{ox}_{pred}(E1)$	$\Delta\Delta E^{ox}_{pred}(E2)$	$\Delta\Delta E^{ox}_{pred}(E3)$	$\Delta\Delta E^{ox}_{pred}(E4)$	$\Delta\Delta E^{ox}_{pred}(E5)$	$\Delta\Delta E^{ox}_{pred}(E6)$	$\Delta\Delta E^{ox}_{cal}$
$[Au_6(dmpp)_4Cl_2]^+$-I2	-0.68	-0.69	-0.69	-0.71	-0.69	-0.73	-0.75
$[Au_6(dmpp)_4Cl]^+$	-0.51	-0.50	-0.54	-0.51	-0.50	-0.56	-0.52
$[Au_6(dmpp)_4Cl]^{2+}$	-0.42	-0.43	-0.39	-0.43	-0.43	-0.41	-0.39
$[Au_6(dmpp)_4]^{2+}$	-0.25	-0.24	-0.24	-0.23	-0.24	-0.23	-0.22
$[Au_6(dmpp)_4]^{3+}$	0.17	0.18	0.22	0.17	0.17	0.22	0.20
$[Au_6(dmpp)_4Cl_2]^{2+}$	0.93	0.93	0.89	0.86	0.92	0.80	0.95
$[Au_8(dppp)_4]^{2+}$	0.38	0.37	0.35	0.43	0.40	0.39	0.38
$[Au_8(dppp)_4]^{3+}$	0.75	0.75	0.75	0.77	0.74	0.78	0.70
$[Au_{23}(c\text{-}C_6)_{16}]^-$	-0.09	-0.09	-0.15	-0.07	-0.09	0.15	-0.13
$[Au_{25}(SMe)_{18}]^-$	-0.30	-0.27	-0.32	-0.30	-0.30	-0.30	-0.21
$[Au_{25}(SMe)_{18}]^0$	-0.09	-0.08	-0.04	-0.09	-0.09	-0.01	-0.11
$[Au_{25}(PET)_{18}]^-$	-0.27	-0.29	-0.29	-0.27	-0.27	-0.27	-0.25
$[Au_{25}(PET)_{18}]^0$	-0.08	-0.10	-0.03	-0.08	-0.07	-0.13	-0.13
R^2	0.9912	0.9936	0.9850	0.9882	0.9909	0.9518	
RMSE	0.04	0.04	0.06	0.05	0.05	0.10	

E1: $\Delta\Delta E^{ox}_{pred}$ = -1.1022*E_{HOMO}+0.0171*N_e-0.0278*N_{Au}-0.0725*N_C+0.0128*N_L-0.0179*$N_{Au(0):Au(I)}$ –4.3618; R^2=0.9912, RMSE=0.04.

E2: $\Delta\Delta E^{ox}_{pred}$ = 1.1038*VIP+0.0781*N_e-0.0680*N_{Au}-0.0332*N_C+0.0716*N_L-0.0298*$N_{Au(0):Au(I)}$-4.9680, R^2=0.9936, RMSE=0.04.

E3: $\Delta\Delta E^{ox}_{pred}$ = -1.0333* E_{HOMO} -0.0208* N_{Au} +0.0235* N_L -4.2756, R^2=0.9850, RMSE=0.06.

E4: $\Delta\Delta E^{ox}_{pred}$ = -1.0823*E_{HOMO}–0.0838*N_C-0.0218*N_L – 4.2367; R2=0.9882; RMSE=0.05.

E5: $\Delta\Delta E^{ox}_{pred}$ = -1.1046* E_{HOMO} – 0.0158*N_{Au} -0.0853*N_C -4.3259, R^2=0.9909, RMSE=0.05.

E6: $\Delta\Delta E^{ox}_{pred}$ = -1.0016* E_{HOMO} +0.0117 * N_C +0.0113*$N_{Au(0):Au(I)}$ -4.2206, R^2=0.9518, RMSE=0.10.

In view of the comparable results of E1 and E2, and the easier availability (and thus lower computational cost) of the HOMO energy than that of VIP, we recommand E1 for future predictions of oxidation potential of other gold clusters.